Real-Time Terahertz Modulation Using Gold-MoS$_2$ Metasurface With Electromagnetically Induced Transparency-Like Resonance

Jianhong Zhang , Zesen Liu , Jiandong Ye , *Member, IEEE*, Weizong Xu , Feng Zhou , Dong Zhou , Rong Zhang , Fangfang Ren , and Hai Lu

Abstract—Terahertz (THz) communication is a rapidly advancing field with applications spanning space exploration, wireless communication, and security checks. Achieving effective intensity modulation of THz radiation is a crucial requirement for THz technology. In this study, we propose an approach to achieve real-time and precise control over THz radiation using a gold split-ring metasurface integrated with MoS$_2$ layers. We demonstrate the emergence of an electromagnetically induced transparency-like resonance through optical pumping, resulting in high-quality THz signal transmission with impressive modulation depth of 81% at 612 GHz. These findings hold great promise for a wide range of THz applications, including sensing, switching, and filtering.

Index Terms—Electromagnetically induced transparency (EIT), modulation, MoS$_2$, terahertz metasurface.

I. INTRODUCTION

THE application of terahertz (THz) radiation, encompassing electromagnetic waves in the frequency range of 0.1–10 THz, has garnered significant attention due to its promising applications in space exploration, wireless communication, and security checks. However, traditional THz devices based on natural materials face challenges in achieving high modulation depth due to their limited interaction with the THz signals [1]. The development of metamaterials has emerged as a breakthrough approach with unique electromagnetic properties, including negative refractive index [2], [3] and perfect lensing [4] capabilities, which are unattainable with conventional materials. This study targets metasurface devices with narrowband resonances for advanced THz modulation [5], [6], [7], stressing the significance of achieving electromagnetically induced transparency-like (EIT-like) resonances [8], [9] with higher quality (Q) factors.

The concept of EIT was introduced theoretically in 1990 [10] and experimental demonstrated in 1991 [11], illustrating a narrow transparency window within a broad absorption region, achieved through quantum interference in three-level atomic systems [12]. In the field of electromagnetism, a similar phenomenon can be achieved with metamaterials, referred to as the EIT-like phenomenon, which was first demonstrated in the THz spectrum in 2008 [13]. Extensive research has been conducted to leverage EIT-like resonances for advanced THz communication devices, including mechanical [14], thermal [15], and electrical [16] approaches. However, these methods exhibit sluggish response, limiting their applicability in ultra-high-speed communication systems. In contrast, optical control, relying on the lifetimes of photo-induced carriers [17], enables ultrafast responses and has rapidly advanced [18], [19], [20], [21]. In this work, we demonstrate the modulation of resonance peak intensity by introducing MoS$_2$ layers into an asymmetric split-ring metasurface, creating an EIT-like resonance as THz signals traverse the engineered structure. Optical pumps with varying pump fluences are applied to enable real-time manipulation of the EIT-like resonance intensity by adjusting the conductivity in the MoS$_2$ layers.

II. SIMULATION METHODS

Fig. 1(a) and (b) depicts the simulation configuration used in CST studio. The THz signal propagates along the z axis, and the configuration of TM (TE) mode is defined as the electric field of incident THz radiation parallel to the x(y) axis. Fig. 1(b) specifies a fundamental unit cell of the hybrid asymmetric split-ring (HASR) metasurface structure. It consists of two distinct arc ring-like arms with two gaps overlaid by MoS$_2$ thin films. The periods along x(y)-axis are both $p = 500\ \mu$m. The gap is denoted as g and the perpendicular distance between the gap center and the ring center is represented as d. The outer radius is $R = 140\ \mu$m. The difference between R and the inner radius r is denoted by w. In the diagram, the color scheme distinguishes different materials: the blue segment signifies the sapphire substrate with a thickness of $t_s = 5\ \mu$m and its dielectric constant is set in accordance with [22], the yellow portion represents gold with a thickness of $t_m = 200$ nm, and the red section symbolizes MoS$_2$ thin films with a length of a and a thickness of $t = 5$ nm, approximately corresponding to 7 layers [23]. The
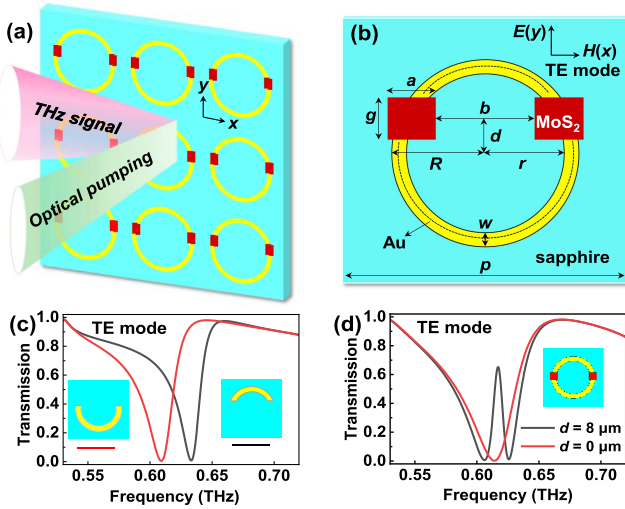
Fig. 1. (a) Simulation configuration of the HASR metasurface. (b) Schematic of a unit cell. (c) Transmission spectra of the first structure (solely upper-arm array) and the second structure (solely lower-arm array). (d) Transmission spectra of the third structure with $d = 0$ or 8 μm.
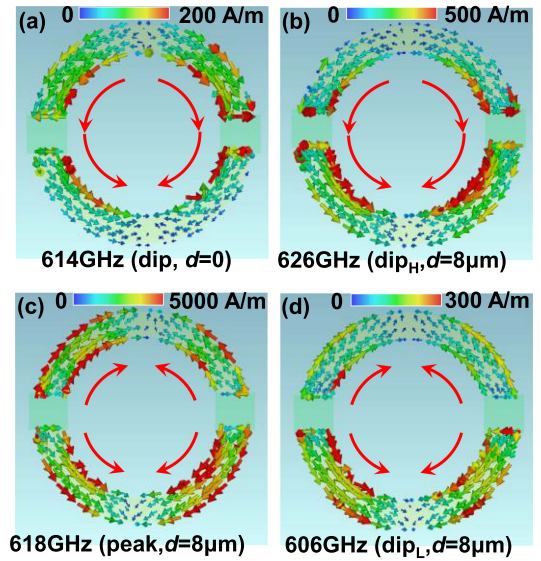

Fig. 2. Distributions of surface current at transmission resonance peak or dips observed in Fig. 1(d): (a) transmission dip at 614 GHz when $d = 0$, (b) transmission dip at 626 GHz (dip$_H$), (c) EIT transmission peak at 618 GHz, and (d) transmission dip at 606 GHz (dip$_L$) when $d = 8$ μm.

distance between two MoS$_2$ films is denoted by b. Here, MoS$_2$ is chosen due to its proper bandgap of 1.29 eV to over 1.9 eV [24], which offers the advantage of modulating carrier density and conductivity in response to optical stimuli using a commonly used laser wavelength. A possible fabrication process for the proposed HASR metasurface is illustrated in the Supplementary Materials.

To introduce changes in the conductivity of MoS$_2$, an optical laser operating at an excitation wavelength of 522 nm is concurrently employed [25]. This particular alteration cannot be directly implemented in CST. Instead, the properties of MoS$_2$ are characterized using the Drude model, providing the ability to define the plasma frequency (ω_p). The relationship between the plasma frequency and carrier density is expressed as $\omega_p^2 = ne^2/(\varepsilon_0 m*) \times 10^6$, where the elementary charge $e = 1.6 \times 10^{-19}$ C, the vacuum permittivity $\varepsilon_0 = 8.85 \times 10^{-12}$ F/m, and the effective mass of MoS$_2$ $m* = 0.58 \times 9.1 \times 10^{-31}$ kg [26], respectively. Here, n refers to the volume carrier density in the unit of cm^{-3}. It is worth noting that when referring to *carrier density* in MoS$_2$, we are specifically addressing surface density, given the two-dimensional (2D) nature of MoS$_2$. To account for this, we approximate the volume density as $n = n_{2D}/t$, where t represents the thickness of MoS$_2$. In Drude model, the dielectric constant at high frequency limit (ε_∞) and collision frequency (γ), are set as $\varepsilon_\infty = 11.475$ [26] and $\gamma = 6.0629 \times 10^{13}$ s^{-1} based on the equation $\gamma = e/(\mu m*)$ [27], respectively. Here, μ represents the mobility of MoS$_2$, which is set as 50 cm^2/(V·s) according to [28]. During the simulation, the lower limit of n is set as 2 $\times 10^{15}$ cm^{-3}, equivalent to $n_{2D} = 1 \times 10^9$ cm^{-2} based on the approximation formula, to replicate conditions without optical pumping [29]. The upper limit of n is set as 1×10^{20} cm^{-3}, aligning with observations in [30], which corresponds to $n_{2D} = 5 \times 10^{13}$ cm^{-2} and optical pump fluence of 20.4 mJ/cm^2 according to the ABC model [31], [32]. The absorption coefficient of few-layer MoS$_2$ is set as 2.8×10^6 cm^{-1} [33]. The conductivity (σ) is acquired in terms of $\sigma = \varepsilon_0 \omega_p^2 (0.5\gamma^3 + 1.5\gamma\omega^2)/(\gamma^2 + \omega^2)^2$ [34].

III. RESULTS AND DISCUSSION

Under TE mode incidence, we conducted a numerical analysis of three metasurface structures on sapphire substrate with the parameters $w = 32$ μm, $d = 8$ μm, $g = 50$ μm, $r = 108$ μm, $a = 52$ μm, and $b = 196$ μm. The first structure comprises an upper-arm array, the second a lower-arm array, and the third a combination of both. The transmission spectra of the first structure (solely upper-arm array) and the second structure (solely lower-arm array) are presented in Fig. 1(c). The upper-arm array displays a resonance at 633 GHz, which red-shifts to 609 GHz for the lower-arm array. This red-shift can be attributed to the elongation of the metal arm, and both resonances are bright modes [35]. Fig. 1(d) shows the transmission spectra of the third structure, which encompasses two scenarios: $d = 0$ resulting in a symmetric structure, and $d = 8$ μm manifesting a HASR metasurface structure. When $d = 0$, a resonance dip emerges at 614 GHz as a consequence of a dipole response that experiences robust coupling with the incident field [36]. Upon adopting the HASR structure, two distinct dips appear at 606 GHz (dip$_L$) and 626 GHz (dip$_H$), accompanied by a sharply defined transparency peak at 618 GHz. This ensemble of features depicts a typical EIT-like resonance profile. The results for TM incidence are not presented since no visible EIT-like resonance is generated within the frequency range of interest.

To clarify the underlying physical mechanism behind the EIT-like resonance observed in the HASR metasurface structure, we conducted calculations to analyze the distribution of surface currents at the transmission resonance peaks or dips. Fig. 2(a)
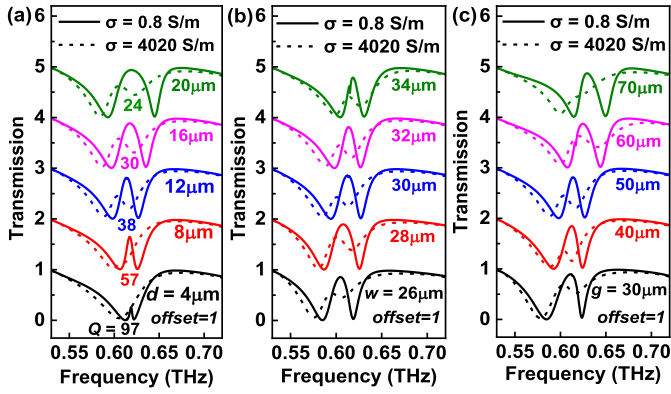
Fig. 3. Transmission spectra of the HASR structure dependent on the structural parameters (a) d, (b) w, and (c) g with conductivity of MoS$_2$ $\sigma = 0.8$ S/m (no optical pump) and 4020 S/m (pump fluence of 20.4 μJ/cm^2).

illustrates the surface current flow occurring at 614 GHz, *i.e.*, the transmission dip when $d = 0$, which unmistakably portrays a dipole nature [37]. In Fig. 2(b), the surface current distribution at 626 GHz (dip$_H$, $d = 8$ μm) is presented, also exhibiting a dipole nature. Fig. 2(c) and (d) show the distributions of surface currents corresponding to the EIT transmission peak at 618 GHz and the dip$_L$ at 606 GHz when $d = 8$ μm, both revealing a quadrupole nature that would remain dormant unless the symmetry of the structure is broken [38], such as in the transition from $d = 0$ to $d = 8$ μm.

Notably, dip$_L$ and dip$_H$ closely align with the resonance dips observed in the lower-arm and upper-arm arrays (Fig. 1(c)). It arises from the interaction between the resonances in the two arms, resulting in the emergence of the induced transparency peak [39]. When $d = 0$, the upper-arm array is effectively identical to the lower-arm array due to their symmetry, resulting in both arms producing the same resonances when exposed to THz signals. However, when d increases to 8 μm, the upper arm shortens while the lower arm lengthens, causing the previously identical resonances to split, with one red-shifting and the other blue-shifting. Consequently, a broad absorption region is observed when $d = 0$, whereas a sharp transparency window emerges when d is 8 μm. Thus, it becomes evident that within the EIT-like resonance profile, dip$_H$ retains its original bright dipole nature, while the emerging peak and concomitant dip$_L$ exhibit a dark quadrupole nature, a result of the strong coupling between the upper and lower arms.

Each structural parameter of the HASR metasurface, including p, d, w, g, R, r, a, b, t_m, or t, exerts an influence on the excitation of EIT-like resonance. They should be optimized to ensure a high Q factor and a significant modulation depth at the resonance frequency. Among these parameters, d plays a crucial role in the manifestation of the EIT-like resonance, while the remaining could potentially induce shifts in the resonance frequency. With $p = 500$ μm, $w = 32$ μm, $g = 50$ μm, $R = 140$ μm, $r = 108$ μm, $a = 52$ μm, $b = 196$ μm, $t_m = 200$ nm, and $t = 5$ nm, we calculate the transmission spectra of the HASR structure by sweeping d from 4 to 20 μm (Fig. 3(a)). This simulation is performed under the condition of a constant conductivity in MoS$_2$,

specifically $\sigma = 0.8$ S/m, corresponding to the case without applying optical pumping [29]. As the value of d increases, the structure adopts an asymmetric configuration, resulting in a rise in the resonance. However, the Q factor experiences a noticeable decrease from 97 to 24 due to the diminishing coupling strength between the upper and lower metal arms (Fig. 3(a)). The Q factor can be computed as $Q = f_0/\Delta f$, where f_0 represents the peak frequency and Δf is the full width at half maximum (FWHM) of the peak [38]. To ensure both a high Q factor and a high transmission at the EIT-like resonance, the value $d = 12$ μm is preferred.

With d fixed at 12 μm, we investigate the influence of the remaining parameters of the HASR structure on the EIT-like resonance, using the values of w and g as examples (depicted in Fig. 3(b) and (c)). For a given set of parameters where $p = 500$ μm, $g = 50$ μm, $R = 140$ μm, $t_m = 200$ nm, and $t = 5$ nm, the EIT-like transmission peak undergoes a blue-shift as w increases. This spectral shift can be attributed to the reduction in the length of the center axis for both the upper and lower arms, which can be visualized as the dark dotted lines in Fig. 1(b). Similarly, as the value of g increases from 30 to 70 μm (Fig. 3(c)), while keeping other parameters $p = 500$ μm, $w = 32$ μm, $R = 140$ μm, $r = 108$ μm, $a = 52$ μm, $b = 196$ μm, $t_m = 200$ nm, and $t = 5$ nm fixed, the EIT-like resonance also experiences a blue-shift due to the decreasing length of both arms. Returning to the scenario of increasing d as depicted in Fig. 3(a), the length of the upper arm decreases, leading to a blueshift in the dip$_H$ frequency. Simultaneously, the length of the lower arm increases, causing a redshift in the dip$_L$ frequency. Ultimately, these opposing shifts in the frequency result in the EIT resonance shift becoming indiscernible. A deeper understanding of how adjusting structural parameters influences EIT resonances can be gleaned from the optical field distribution variation as shown in Figure S1 in the Supplementary Materials.

To further enhance the modulation effect through structural optimization, it is imperative to analyze transmission spectra corresponding to elevated conductivity within the MoS$_2$ layers, such as $\sigma = 4020$ S/m, corresponding to a pump fluence of 20.4 μJ/cm^2 according to ABC model [31], [32]. The objective is to achieve a highest possible difference in transmissivity (ΔT) within the EIT-like transparency region when comparing the cases with and without photoexcitation. By fixing the other structural parameters, we calculate the transmission spectra for the case where conductivity $\sigma = 4020$ S/m by systematically varying the value of d, w, or g, also illustrated in Fig. 3. The EIT-like resonance demonstrates behaviors akin to the case of $\sigma = 0.8$ S/m, albeit with a diminished intensity of the transparency window. This reduction can be attributed to the photoexcitation of free charge carriers within the MoS$_2$ layers, which shunts the metamaterial resonance [17]. Upon reaching $g = 70$ μm, the structure nears symmetry, coupled with a high conductivity of $\sigma = 4020$ S/m, leading to the vanishing of the EIT-like transparency window, as illustrated in Fig. 3(c). The EIT-like resonance disappears as $d = 4$ μm and $\sigma = 4020$ S/m, as shown in Fig. 3(a), which indicates that the slight asymmetry in structure is negligible when carrier density is high enough.
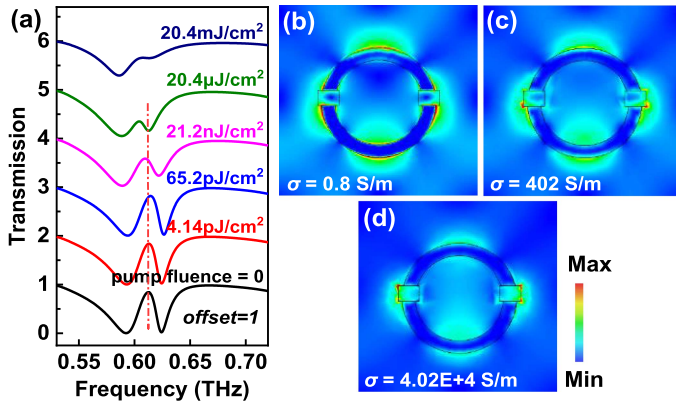
(a)

Fig. 4.   (a) Transmission spectra of HASR structure under optical excitation with varying pump fluences. (b)–(d) Distributions of optical fields (|E|) at EIT-like resonance with MoS$_2$ conductivity $\sigma = 0.8$, 402, and 4.02×10^4 S/m.

Building upon the insights from the discussion regarding Fig. 3, the parameters d, w, and g in the HASR structure can be optimized by comparing the transmissivity difference (ΔT) around EIT-like resonance between conductivity $\sigma = 0.8$ S/m and 4020 S/m. Given that a higher ΔT implies a more preferable modulation effect, we ascertain the optimal values for d, w, and g as 12 μm, 32 μm, and 40 μm, respectively. Notably, the maximum ΔT obtained in this study attains 0.68 around 612 GHz, which suggests that the designed HASR metasurface can exhibit exceptional performance. Finally, the transmission property of the HASR structure is investigated under optical excitation with varying pump fluences as shown in Fig. 4(a). In the absence of photoexcitation, an EIT peak emerges amidst two resonance dips, featuring a transmission amplitude of 0.84 at 612 GHz. As the pump fluence of the pump beam gradually escalates to 20.4 μJ/cm^2 (corresponding to $\sigma = 4020$ S/m), the EIT transmission decreases in magnitude and undergoes a strong modulation. When the pump fluence reaches 20.4 mJ/cm^2 ($\sigma = 4.02 \times 10^4$ S/m), the transparency window almost fades away. Consequently, the transmission spectra accomplish a distinctive on-to-off modulation at 612 GHz characterized by an impressive modulation depth of 81%, achieved by varying the pump fluence from 0 to 20.4 μJ/cm^2. The modulation depth is estimated by $\Delta T/T_0$, where T_0 represents the transmission at EIT peak without optical pump [1]. In this modulation process, the recovery time of excited carriers in MoS$_2$ is approximately in picosecond (ps) range, estimated according to the carrier lifetime of MoS$_2$ [40].

To elucidate this phenomenon comprehensively, we present distributions of the optical field (|E|) at EIT resonance frequencies under varying conductivity of $\sigma = 0.8$, 402, and 4.02×10^4 S/m in Fig. 4(b)–(d). These distributions correspond to distinct levels of photoexcitation pump fluence, delineating the transition from a pronounced EIT peak to its disappearance. In the absence of optical pumping, as shown in Fig. 4(b), the MoS$_2$ layers predominantly exhibit dielectric characteristics, while the two metal arms manifest minimal damping. The optical field predominantly concentrates along the surface of metal arms, and the optical field within the MoS$_2$ is markedly suppressed. Upon photoexcitation, the conductivity and carrier density within the

MoS$_2$ layers gradually elevate, resulting in a redistribution of the optical field in the HASR structure. This transformation is evident in Fig. 4(c), wherein the optical field along metal arms experiences attenuation, while the optical field within the MoS$_2$ becomes more pronounced. At an excitation level of 20.4 mJ/cm^2 ($\sigma = 4.02 \times 10^4$ S/m), as shown in Fig. 4(d) the optical field undergoes further redistribution in a similar manner. From these observations, it is evident that the modulation of the EIT resonance fundamentally stems from the optically controllable conductivity and carrier density of the MoS$_2$ layers, attributed to the photodoping effect. Furthermore, the underlying origin can also be linked to the adjusted Fermi level of MoS$_2$ through elevated carrier density, akin to research conducted on graphene [41], [42], [43], [44].

IV. CONCLUSION

In conclusion, EIT-like resonance is induced in HASR metasurface structures based on the destructive interference between the bright dipole mode and the dark quadrupole mode. The transmission spectra exhibit high Q factors reaching 97, and the characteristics can be finely tuned by adjusting the structural parameters and symmetry of the two metal arms. When carrier density/conductivity in MoS$_2$ increments due to optical pumping, it leads to a substantial modulation of the transmission resonance peak intensity. This modulation effect, quantified by ΔT, can reach a significant value of 0.68, corresponding to a modulation depth of 81%. These findings underscore the potential of HASR structures in the development of high-performance THz sensors, switches, and filters, opening up exciting possibilities for advanced optical applications.

REFERENCES

[1] Z. Wang et al., "Recent progress in terahertz modulation using photonic structures based on two-dimensional materials," *InfoMat*, vol. 3, no. 10, pp. 1110–1133, 2021, doi: 10.1002/inf2.12236.

[2] R. A. Shelby, D. R. Smith, and S. Schultz, "Experimental verification of a negative index of refraction," *Science*, vol. 292, no. 5514, pp. 77–79, Apr. 2001, doi: 10.1126/science.1058847.

[3] M. Liu et al., "Temperature-controlled optical activity and negative refractive index," *Adv. Funct. Mater.*, vol. 31, no. 14, Apr. 2021, Art. no. 2010249, doi: 10.1002/adfm.202010249.

[4] J. B. Pendry, "Negative refraction makes a perfect lens," *Phys. Rev. Lett.*, vol. 85, no. 18, pp. 3966–3969, Oct. 2000, doi: 10.1103/Phys-RevLett.85.3966.

[5] H. T. Chen, W. J. Padilla, J. M. O. Zide, A. C. Gossard, A. J. Taylor, and R. D. Averitt, "Active terahertz metamaterial devices," *Nature*, vol. 444, no. 7119, pp. 597–600, Nov. 2006, doi: 10.1038/nature05343.

[6] M. Liu et al., "Switchable chiral mirrors," *Adv. Opt. Mater.*, vol. 8, no. 15, Aug. 2020, Art. no. 2000247, doi: 10.1002/adom.202000247.

[7] N. Kumar, S. K. Ghosh, and S. Bhattacharyya, "Thermally switchable metasurface for controlling transmission in the THz-gap," *Plasmonics*, Nov. 2023, doi: 10.1007/s11468-023-02115-1.

[8] G. X. Guo et al., "Programmable graphene metasurface for terahertz propagation control based on electromagnetically induced transparency," *Carbon*, vol. 208, pp. 345–354, May 2023, doi: 10.1016/j.carbon.2023.03.062.

[9] Q. W. Wang et al., "Nonlinear terahertz generation: Chiral and achiral meta-atom coupling," *Adv. Funct. Mater.*, vol. 33, no. 29, Jul. 2023, Art. no. 2300639, doi: 10.1002/adfm.202300639.

[10] S. E. Harris, J. E. Field, and A. Imamoglu, "Nonlinear optical processes using electromagnetically induced transparency," *Phys. Rev. Lett.*, vol. 64, no. 10, pp. 1107–1110, Mar. 1990, doi: 10.1103/PhysRevLett.64.1107.

[11] K. J. Boller, A. Imamoglu, and S. E. Harris, "Observation of electromagnetically induced transparency," *Phys. Rev. Lett.*, vol. 66, no. 20, pp. 2593–2596, May 1991, doi: 10.1103/PhysRevLett.66.2593.

[12] S. E. Harris, "Electromagnetically induced transparency," *Phys. Today*, vol. 50, no. 7, pp. 36–42, Jul. 1997, doi: 10.1063/1.881806.

[13] S. Zhang, D. A. Genov, Y. Wang, M. Liu, and X. Zhang, "Plasmon-induced transparency in metamaterials," *Phys. Rev. Lett.*, vol. 101, no. 4, Jul. 2008, Art. no. 047401, doi: 10.1103/PhysRevLett.101.047401.

[14] P. Pitchappa, M. Manjappa, C. P. Ho, R. Singh, N. Singh, and C. Lee, "Active control of electromagnetically induced transparency analog in terahertz MEMS metamaterial," *Adv. Opt. Mater.*, vol. 4, no. 4, pp. 541–547, Apr. 2016, doi: 10.1002/adom.201500676.

[15] W. T. Zhang, H. Y. Li, S. Yin, W. Huang, X. T. Shi, and Y. T. Zhang, "Active thermal modulation of electromagnetically induced transparency at terahertz frequencies," *Opt. Eng.*, vol. 59, no. 12, Dec. 2020, Art. no. 127111, doi: 10.1117/1.Oe.59.12.127111.

[16] S. J. Kindness et al., "Graphene-integrated metamaterial device for all-electrical polarization control of terahertz quantum cascade lasers," *ACS Photon.*, vol. 6, no. 6, pp. 1547–1555, Jun. 2019, doi: 10.1021/acsphotonics.9b00411.

[17] H. T. Chen et al., "Ultrafast optical switching of terahertz metamaterials fabricated on ErAs/GaAs nanoisland superlattices," *Opt. Lett.*, vol. 32, no. 12, pp. 1620–1622, Jun. 2007, doi: 10.1364/ol.32.001620.

[18] K. M. Devi, A. Jana, A. Punjal, N. Acharyya, S. S. Prabhu, and D. R. Chowdhury, "Polarization-independent tunable terahertz slow light with electromagnetically induced transparency metasurface," *New J. Phys.*, vol. 24, no. 9, Sep. 2022, Art. no. 093004, doi: 10.1088/1367-2630/ac8ac4.

[19] Q. Xu et al., "Meta-optics inspired surface plasmon devices," *Photon. Insights*, vol. 2, no. 1, 2023, Art. no. R02, doi: 10.3788/pi.2023.R02.

[20] M. Manjappa, Y. K. Srivastava, L. Q. Cong, I. Al-Naib, and R. Singh, "Active photoswitching of sharp Fano resonances in THz metadevices," *Adv. Mater.*, vol. 29, no. 3, Jan. 2017, Art. no. 1603355, doi: 10.1002/adma.201603355.

[21] L. Q. Cong, Y. K. Srivastava, H. F. Zhang, X. Q. Zhang, J. G. Han, and R. Singh, "All-optical active THz metasurfaces for ultrafast polarization switching and dynamic beam splitting," *Light-Sci. Appl.*, vol. 7, Jul. 2018, Art. no. 28, doi: 10.1038/s41377-018-0024-y.

[22] D. Grischkowsky, S. Keiding, M. Vanexter, and C. Fattinger, "Far-infrared time-domain spectroscopy with terahertz beams of dielectrics and semiconductors," *J. Opt. Soc. Am. B-Opt. Phys.*, vol. 7, no. 10, pp. 2006–2015, Oct. 1990, doi: 10.1364/josab.7.002006.

[23] H. Qiu et al., "Hopping transport through defect-induced localized states in molybdenum disulphide," *Nature Commun.*, vol. 4, Oct. 2013, Art. no. 2642, doi: 10.1038/ncomms3642.

[24] K. F. Mak, C. Lee, J. Hone, J. Shan, and T. F. Heinz, "Atomically thin MoS$_2$: A new direct-gap semiconductor," *Phys. Rev. Lett.*, vol. 105, no. 13, Sep. 2010, Art. no. 136805, doi: 10.1103/PhysRevLett.105.136805.

[25] W. Z. Xu et al., "Vertically emitting indium phosphide nanowire lasers," *Nano Lett.*, vol. 18, no. 6, pp. 3414–3420, Jun. 2018, doi: 10.1021/acs.nanolett.8600334.

[26] W. R. Zhu et al., "MoS$_2$ broadband coherent perfect absorber for terahertz waves," *IEEE Photon. J.*, vol. 8, no. 6, Dec. 2016, Art. no. 5502207, doi: 10.1109/jphot.2016.2633571.

[27] D. Shrekenhamer et al., "High speed terahertz modulation from metamaterials with embedded high electron mobility transistors," *Opt. Exp.*, vol. 19, no. 10, pp. 9968–9975, May 2011, doi: 10.1364/oe.19.009968.

[28] S. Poncé, W. B. Li, S. Reichardt, and F. Giustino, "First-principles calculations of charge carrier mobility and conductivity in bulk semiconductors and two-dimensional materials," *Rep. Prog. Phys., Rev.*, vol. 83, no. 3, Mar. 2020, Art. no. 036501, doi: 10.1088/1361-6633/ab6a43.

[29] M. D. Siao et al., "Two-dimensional electronic transport and surface electron accumulation in MoS$_2$," *Nature Commun.*, vol. 9, Apr. 2018, Art. no. 1442, doi: 10.1038/s41467-018-03824-6.

[30] D. P. Khatua et al., "Ultrafast carrier dynamics in a monolayer MoS$_2$ at carrier densities well above Mott density," *J. Phys.-Condes. Matter*, vol. 34, no. 15, Apr. 2022, Art. no. 155401, doi: 10.1088/1361-648X/ac4dbf.

[31] Y. S. Yoo, T. M. Roh, J. H. Na, S. J. Son, and Y. H. Cho, "Simple analysis method for determining internal quantum efficiency and relative recombination ratios in light emitting diodes," *Appl. Phys. Lett.*, vol. 102, no. 21, May 2013, Art. no. 211107, doi: 10.1063/1.4807485.

[32] O. Salehzadeh, N. H. Tran, X. Liu, I. Shih, and Z. Mi, "Exciton kinetics, quantum efficiency, and efficiency droop of monolayer MoS$_2$ light-emitting devices," *Nano Lett.*, vol. 14, no. 7, pp. 4125–4130, Jul. 2014, doi: 10.1021/nl5017283.

[33] J. Y. Kwak, "Absorption coefficient estimation of thin MoS$_2$ film using attenuation of silicon substrate Raman signal," *Results Phys.*, vol. 13, Jun. 2019, Art. no. 102202, doi: 10.1016/j.rinp.2019.102202.

[34] Y. K. Srivastava et al., "MoS$_2$ for ultrafast all-optical switching and modulation of THz fano metaphotonic devices," *Adv. Opt. Mater.*, vol. 5, no. 23, Dec. 2017, Art. no. 1700762, doi: 10.1002/adom.201700762.

[35] T. Zhou, S. G. Chen, X. J. Zhang, X. Zhang, H. Hu, and Y. Wang, "Electromagnetically induced transparency based on a carbon nanotube film terahertz metasurface," *Opt. Exp.*, vol. 30, no. 9, pp. 15436–15445, Apr. 2022, doi: 10.1364/oe.457768.

[36] R. Singh, I. Al-Naib, W. Cao, C. Rockstuhl, M. Koch, and W. L. Zhang, "The Fano resonance in symmetry broken terahertz metamaterials," *IEEE Trans. THz Sci. Technol.*, vol. 3, no. 6, pp. 820–826, Nov. 2013, doi: 10.1109/tthz.2013.2285498.

[37] C. Kyaw et al., "Polarization-selective modulation of supercavity resonances originating from bound states in the continuum," *Commun. Phys.*, vol. 3, no. 1, Nov. 2020, Art. no. 212, doi: 10.1038/s42005-020-00453-8.

[38] W. Cao, R. Singh, I. A. I. Al-Naib, M. X. He, A. J. Taylor, and W. L. Zhang, "Low-loss ultra-high-*Q* dark mode plasmonic Fano metamaterials," *Opt. Lett.*, vol. 37, no. 16, pp. 3366–3368, Aug. 2012, doi: 10.1364/ol.37.003366.

[39] K. Ren, Y. Zhang, X. B. Ren, Y. M. He, and Q. Han, "Polarization-sensitive and active controllable electromagnetically induced transparency in U-shaped terahertz metamaterials," *Front. Optoelectron.*, vol. 14, no. 2, pp. 221–228, Jun. 2021, doi: 10.1007/s12200-019-0921-6.

[40] P. Y. Yuan, J. Liu, R. D. Wang, and X. W. Wang, "The hot carrier diffusion coefficient of sub-10 nm virgin MoS$_2$ uncovered by non-contact optical probing," *Nanoscale*, vol. 9, no. 20, pp. 6808–6820, May 2017, doi: 10.1039/c7nr02089a.

[41] L. P. Xia et al., "Multi-mode graphene based terahertz amplitude modulation enhanced by hollow cross H-structured metasurface," *Physica Scripta*, vol. 94, no. 12, Dec. 2019, Art. no. 125701, doi: 10.1088/1402-4896/ab1bfe.

[42] Q. Li et al., "Monolayer graphene sensing enabled by the strong Fano-resonant metasurface," *Nanoscale*, vol. 8, no. 39, pp. 17278–17284, 2016, doi: 10.1039/c6nr01911k.

[43] S. Y. Xiao et al., "Strong interaction between graphene layer and fano resonance in terahertz metamaterials," *J. Phys. D-Appl. Phys.*, vol. 50, no. 19, May 2017, Art. no. 195101, doi: 10.1088/1361-6463/aa69b1.

[44] Q. S. Li et al., "Gate-tuned graphene meta-devices for dynamically controlling terahertz wavefronts," *Nanophotonics*, vol. 11, no. 9, pp. 2085–2096, May 2022, doi: 10.1515/nanoph-2021-0801.